

3D Mesoporous Graphene: CVD Self-Assembly on Porous Oxide Templates and Applications in High-Stable Li-S Batteries

Jia-Le Shi, Cheng Tang, Hong-Jie Peng, Lin Zhu, Xin-Bing Cheng, Jia-Qi Huang, Wancheng Zhu, and Qiang Zhang*

A nanostructured carbon with high specific surface area (SSA), tunable pore structure, superior electrical conductivity, mechanically robust framework, and high chemical stability is an important requirement for electrochemical energy storage. Porous graphene fabricated by chemical activation and liquid etching has a high surface area but very limited volume of electrochemically accessible mesopores. Herein, an effective strategy of *in situ* formation of hierarchically mesoporous oxide templates with small pores induced by Kirkendall diffusion and large pores attributed to evaporation of deliberately introduced volatile metal is proposed for chemical vapor deposition assembly of porous graphene frameworks (PGFs). The PGFs inherit the hierarchical mesoporous structure of the templates. A high SSA of $1448 \text{ m}^2 \text{ g}^{-1}$, 91.6% of which is contributed by mesopores, and a mesopore volume of $2.40 \text{ cm}^3 \text{ g}^{-1}$ are attained for PGFs serving as reservoirs of ions or active materials in electrochemical energy storage applications. When the PGFs are applied in lithium-sulfur batteries, a very high sulfur utilization of 71% and a very low fading rate of $\approx 0.04\%$ per cycle after the second cycle are achieved at a current rate of 1.0 C. This work provides a general strategy for the rational construction of mesoporous structures induced by a volatile metal, with a view toward the design of hierarchical nanomaterials for advanced energy storage.

1. Introduction

Nanostructured carbon materials play a critical role in the sustainable development of energy storage, environmental protection, and information technology.^[1–3] For instance,

J.-L. Shi, C. Tang, H.-J. Peng, L. Zhu, X.-B. Cheng,
Prof. J.-Q. Huang, Prof. Q. Zhang
Beijing Key Laboratory of Green Chemical Reaction
Engineering and Technology
Department of Chemical Engineering
Tsinghua University
Beijing 100084, China
E-mail: zhang-qiang@mails.tsinghua.edu.cn

L. Zhu, Prof. W. C. Zhu
Department of Chemical Engineering
Qufu Normal University
Shandong 273165, China
DOI: 10.1002/sml.201501467



electrodes for supercapacitors are mainly carbon nanomaterials, and carbon-based anodes have been widely applied in commercial lithium ion batteries. Recently emerging lithium-sulfur (Li-S) batteries based on multielectron chemical conversion reactions have been of great concern, as well as the carbon-sulfur composite cathodes in Li-S batteries.^[4] In general, the electrochemical reaction can only take place at the interface where the electron pathway and the ion diffusion channel meet. Carbon is mostly demonstrated as the electron highway, while the interconnected pores within carbon materials are employed as the ion diffusion channels. Therefore, a carbon material with high electrical conductivity, high specific surface area (SSA), tunable pore structure, mechanically robust framework, and high chemical stability is an important requirement for advanced electrochemical energy storage.

A conductive agent is always required to form a 3D conductive electrode in energy applications. Therefore, various kinds of carbon materials have been proposed for

electrochemical energy storage. On the one hand, porous carbon (e.g., activated carbon, microporous carbon, mesoporous carbon, hierarchically porous carbon) usually has very high SSA and tunable pore structure; however, its electrical conductivity is commonly less than $10^{-4} \text{ S cm}^{-1}$.^[1-3] On the other hand, sp^2 carbon (e.g., graphene, carbon nanotubes (CNTs)) is strongly considered for its high electrical conductivity (larger than 1 S cm^{-1}), robust mechanical framework, and high chemical stability;^[1] however, graphene materials prefer to pack with each other, while CNTs are inclined to form bundles. Therefore, the specific surface area of common sp^2 carbon is mostly less than $500 \text{ m}^2 \text{ g}^{-1}$. Introducing spacers to separate the building blocks of CNTs and/or graphene is an important strategy. For instance, engineering graphene wrinkles as spacers is a facile route to obtain crumpled graphene with high surface area and improved capacitance;^[5,6] CNTs and graphene were sandwiched into a hybrid structure with 3D electrical conductive networks and a large exposed surface area.^[7,8] We also proposed an unstacked double-layer templated graphene (DTG) in which ultrashort CNT (<10 nm) served as spacers to pillar two layers of graphene.^[9] However, a careful combination of porous carbon and sp^2 carbon into advanced carbon materials that inherit the desirable merits of the parent materials is still required to fully demonstrate the potential of carbon materials for energy storage.

Porous graphene is a promising platform since the interconnected graphene unit can serve as more efficient electron pathways than amorphous carbon and, abundant meso-/micropores are employed as ion diffusion channels. The most accepted method of obtaining microporous graphene is KOH activation, which generates abundant micropores in the resultant carbon.^[10] However, mesoporous graphene is difficult to achieve due to the harsh reaction of KOH activation under high temperature. The casting of carbonaceous liquid/gas sources into ordered scarified frameworks, which are formed by structured solids (known as hard templates) or colloidal assemblies (known as soft templates), is another notably effective strategy to introduce pores into the carbon matrix.^[6]

Focusing on hard-template synthesis, carbon materials with graphitic or even graphene-wall porous structure have recently been pursued.^[6,11-13] High temperature (>900 °C) chemical vapor deposition (CVD) is widely accepted for producing high-quality graphene. It is also applied for fabricating porous carbon with graphene structure (porous graphene), not only because of the availability of tunable synthesis parameters for accurate casting, but also the high quality of the sp^2 -carbon structure obtained. The use of metals (e.g., Ni^[14]), metal oxides (e.g., MgO,^[15] MgAl_2O_4 ,^[9] zeolites,^[2] etc.), and sulfides (e.g., Ni_3S_2 ^[16]) as hard templates has been explored to produce porous graphene. The pore size distribution depends on the original porous structure of the inorganic templates, which can be well tuned by rationally formulating the composition and structural evolution of the templates. Very recently, the use of sacrificial

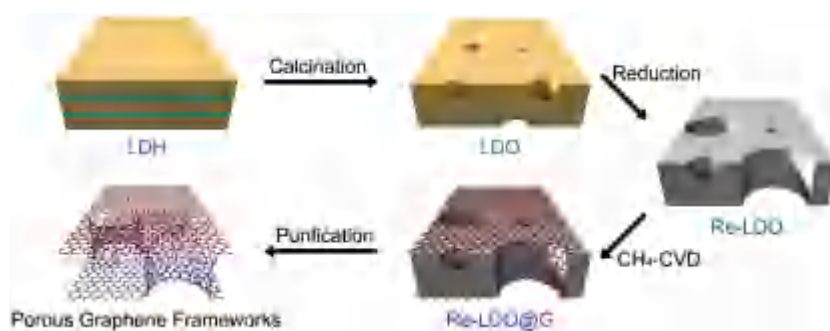


Figure 1. Schematic for PGF fabrication. A hierarchically porous oxide flake with small pores induced by Kirkendall diffusion during calcination and large pores attributed to volatile metal evaporation during subsequent reduction was used as a hard template to cast graphene. The PGF with large mesopores was obtained by chemical removal of the oxide template.

oxide scaffolds for in situ removal of all pore-forming components through associated reactions was of high concern.^[11] The delicate structure modulation of hard templates is the core for graphene casting on oxide templates. However, few mesoporous templates with controllable organized structures have yet been proposed. In some cases, the prepared porous carbon suffered structural collapse as the size of template-generated pores was too large.^[12,13] Due to the harsh conditions of CVD growth at high temperature, and the template removal by strong acid/alkali treatment, a robust inorganic template with excellent structural stability and reproducibility is of paramount importance for the process.

In this contribution, we propose an in situ route to fabricate hierarchically mesoporous oxide templates, in which small pores are introduced by Kirkendall diffusion during calcination of precursors and large pores are attributed to evaporation of volatile metal during subsequent reduction (**Figure 1**). 3D graphene with large mesopores was cast onto metal oxides through facile CVD. The as-obtained porous graphene frameworks (PGFs) composed of abundant interconnected mesopores were employed as conductive scaffolds to host sulfur for lithium ion storage. Compared with other energy storage routes (e.g., supercapacitors, flow redox batteries, lithium ion batteries), the Li-S batteries afford a very high energy density of 2600 Wh kg^{-1} theoretically and $500\text{--}700 \text{ Wh kg}^{-1}$ potentially at low costs.^[4] As a proof-of-concept, Li-S batteries were selected as a probe system to demonstrate the advantages and huge potential of PGFs for energy applications.

2. Results and Discussion

2.1. Oxide Templates with Large Mesopores

A Zn-Mg-Al system was adopted as a model for the rational combination of Kirkendall diffusion and reduction-induced metal evaporation toward hierarchical oxide templates for CVD self-assembly of 3D porous graphene. $\text{Mg}_2\text{Zn}_{0.1}\text{Al}$ -layered double hydroxide (LDH) flakes were selected as template precursors. LDHs are a class of ionic lamellar compounds made up of positively charged brucite

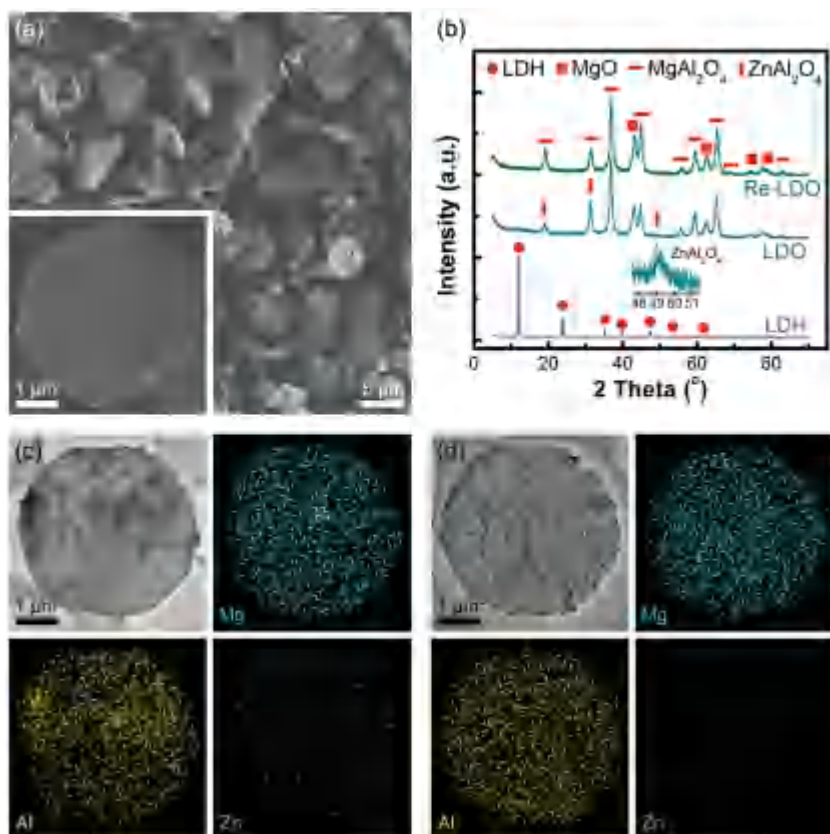


Figure 2. Characterization of the LDH, LDO, and Re-LDO. a) SEM image of the LDH, b) XRD spectra of the LDH, LDO, and Re-LDO, TEM image, and EDX mappings of c) the LDO and d) Re-LDO.

(Mg(OH)₂)-like layers with an interlayer region containing charge-balancing anions and solvent molecules.^[17] Most metal elements (e.g., Mg, Al, Fe, Co, Ni, Cu, Zn, etc.) can be well-dispersed at an atomic level in the inorganic layers.^[18]

Herein, Mg₂Zn_{0.1}Al-LDH flakes with a lateral size of ≈4.0 μm were prepared using a facile urea-assisted coprecipitation (**Figure 2a**). The powder X-ray diffraction (XRD) pattern (**Figure 2b**) reveals crystallization of the as-prepared LDHs with intercalation of carbonates as a series of low angle (001) characteristic peaks. During calcination in an inert atmosphere, Mg₂Zn_{0.1}Al-CO₃-LDHs gradually underwent the removal of free and interlayer H₂O molecules, dehydroxylation of inorganic layers, decomposition of interlayer CO₃²⁻, and formation of spinel phases (MgAl₂O₄ and ZnAl₂O₄) (**Figure S1**, Supporting Information). The hydroxide-like LDH phase was topotactically transformed into a mixed metal oxide phase containing MgO, MgAl₂O₄, and ZnAl₂O₄, giving so-called Mg₂Zn_{0.1}Al-LDO (later shortened to LDO) (**Figure 2b**). The plate-like morphology of the LDH flakes and the atomic level dispersion of Mg, Zn, and Al were well preserved in the LDO templates (**Figure 2c**).

After further reduction of the LDO templates at 950 °C in a H₂ atmosphere, the in situ reduced Zn nanoparticles were immediately vaporized since the bulk Zn metal has a low boiling point of 907 °C. Consequently, Zn element was fully removed from the solid phase and Zn-free LDO templates

(denoted as Re-LDOs) were obtained. Meanwhile, the characteristic peak of the (311) plane of ZnAl₂O₄ at 2θ = 49.07° totally vanished due to the reduction (**Figure 2b**), while the reduced Zn metal completely volatilized as indicated by the energy-dispersive X-ray spectroscopy (EDX) mapping results (**Figure 2d**). The extraction of Zn from the inorganic flake rendered a greater abundance of pores while the remaining MgO and MgAl₂O₄ phases still persisted without any structural collapse due to their extraordinary thermal stability at high-temperature, which far exceeded the pure sacrificial templates of bare zinc oxides.

During the topotactic transformation from Mg₂Zn_{0.1}Al-LDHs to LDOs, there were large quantities of Kirkendall voids with a size of 3–15 nm on the Mg₂Zn_{0.1}Al-LDO, which was driven by the difference in diffusivities of Mg, Zn, and Al atoms along with the release of H₂O and CO₂ molecules (**Figure 3a**).^[19] The Kirkendall voids were distributed on the LDO flakes as shallow pits while no void across the whole flake can be observed. However, after reduction of ZnAl₂O₄ and volatilization of Zn from the LDO laminate, some Kirkendall voids were deepened and broadened with their size extended to 10–20 nm (**Figure 3b**). Holes

throughout the whole LDO flake exhibited sizes larger than 15 nm. Rather than an integrated 2D laminate morphology, the Re-LDOs possessed secondary building blocks of interconnected MgO and MgAl₂O₄ nanoparticles to assemble into a hierarchical 3D porous architecture. N₂ physisorption indicated the quantitative information of the pore structure. Re-LDOs exhibited higher N₂ sorption volume than LDOs (**Figure 3c**). The SSA resolved from Brunauer–Emmett–Teller method (SSA_{BET}) LDOs and Re-LDOs were 29 and 39 m² g⁻¹, and the corresponding pore volumes were 0.07 and 0.11 cm³ g⁻¹, respectively. All these improvements on surface area and pore volume were ascribed to the large mesopores of Re-LDOs after in situ Zn removal (**Figure 3d**). The large mesopores of Re-LDO templates are highly desirable for replicating more accessible mesopores of templated-CVD 3D graphene.

2.2. CVD Self-Assembly of Graphene on Porous Oxide Templates

The mesoporous Re-LDO flakes with oxygen-terminated surfaces are able to catalyze CH₄ decomposition at a high temperature of 950 °C to reorganize cracked carbon fragments into the graphene lattice. After the CVD of CH₄ onto the Re-LDO flakes, the as-obtained Re-LDO@graphene (Re-LDO@G) composites exhibited similar plate-like

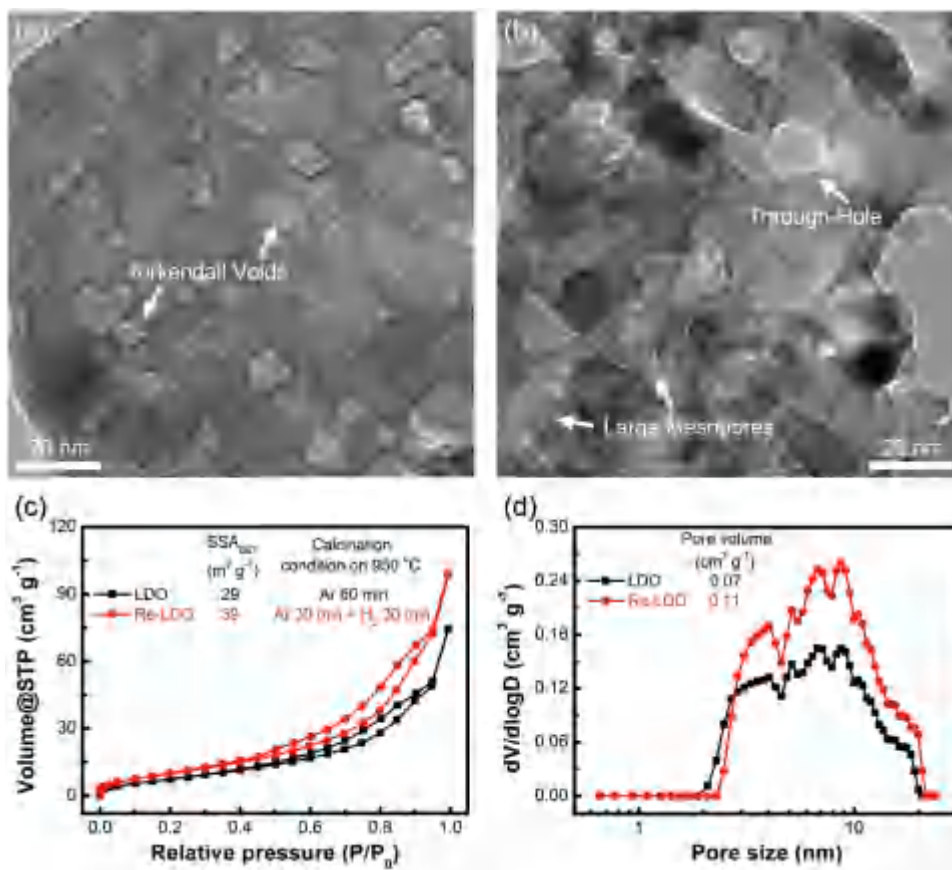


Figure 3. Porous structure characterization of the LDO and Re-LDO. TEM images of a) the LDO and b) Re-LDO, c) N₂ Isotherms of the LDO and Re-LDO, and d) pore size distributions derived from isothermal adsorption plots.

morphology to LDH precursors (inset of Figure 4a). Except for the XRD patterns of MgO and MgAl₂O₄ as in Re-LDOs, the characteristic diffraction peak of graphite at 26.4° was indiscernible, indicating the few-layer nature of deposited graphene (Figure 4a). Perfect alignments of the (111) and (220) lattice with *d*-spacings of 0.47 and 0.28 nm

unambiguously indicated the MgAl₂O₄ spinel phase, where the deposited ultrathin graphene layer tightly wrapped on the fringe of nanoparticle templates (Figure 4b). But the interparticle mesopores of Re-LDOs can still be clearly observed when not filled with carbon. The interconnected mesoporous structure was thereby preserved.

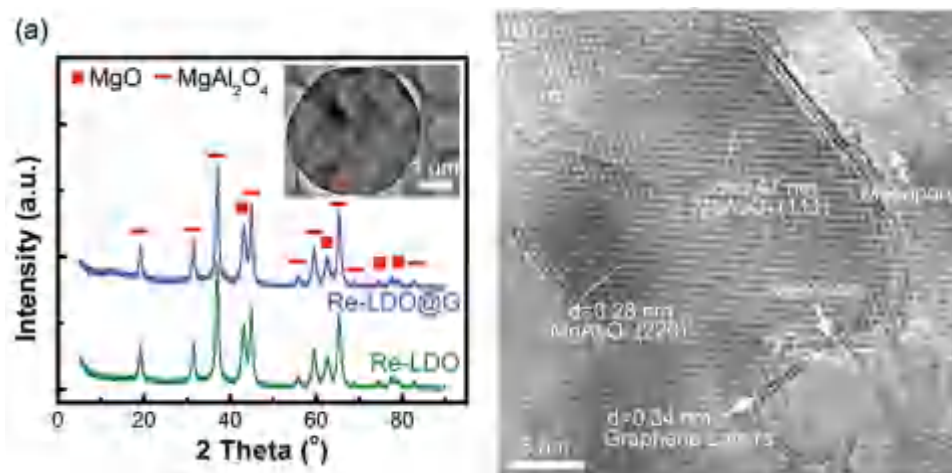


Figure 4. Characterization of the Re-LDO@G. a) XRD spectra of the Re-LDO and Re-LDO@G (inset of (a) is the TEM image of the Re-LDO@G), b) high resolution TEM image of the Re-LDO@G.

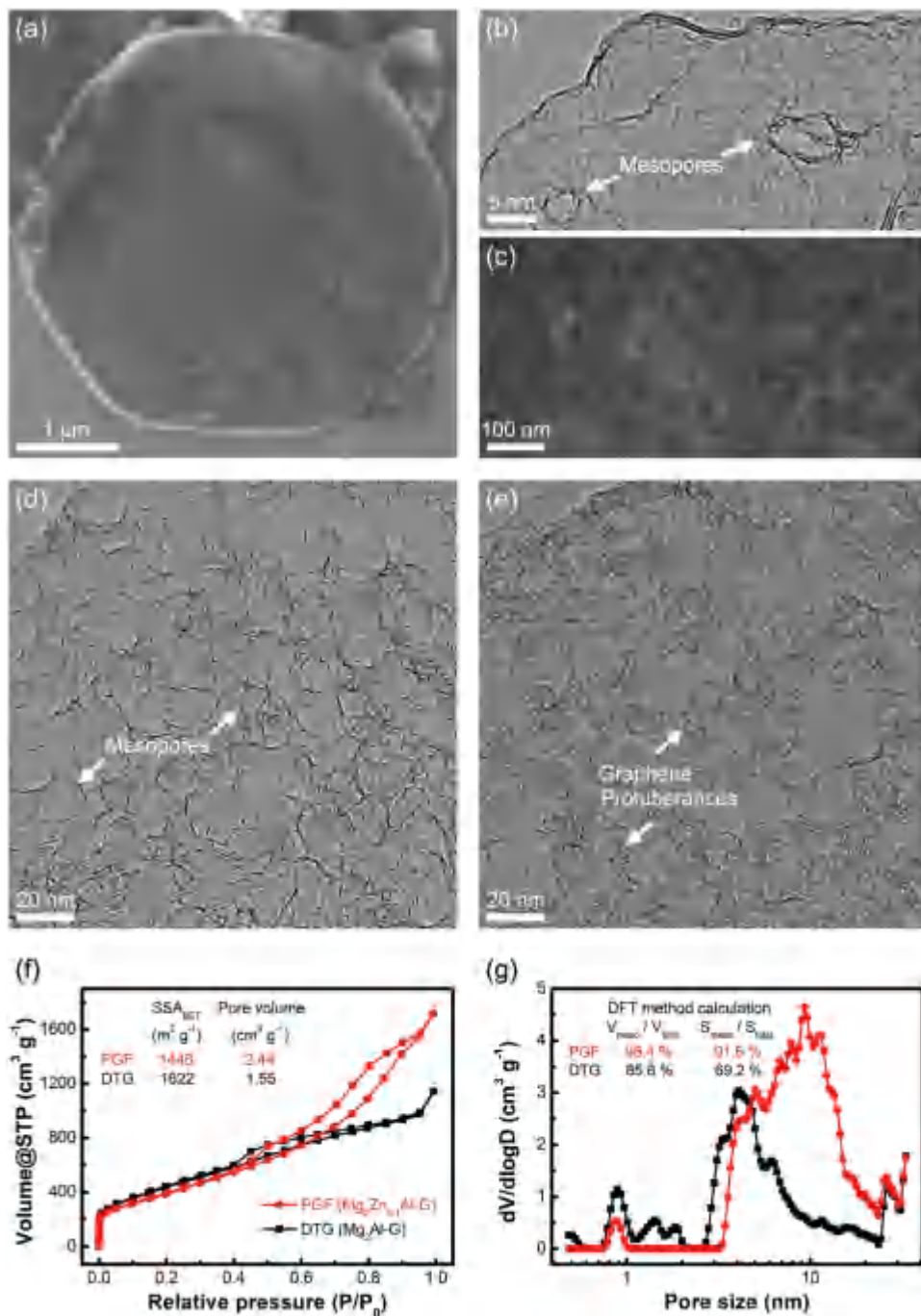


Figure 5. Characterization of the PGF. a) SEM and b) TEM images of the PGF, c) high resolution SEM, and d) TEM images of PGF indicating large mesopores. e) TEM image of DTG, f) N₂ isotherms of the PGF and DTG, g) pore size distributions derived from isothermal adsorption plots.

2.3. Characterization of the 3D Graphene with Large Mesopores

The removal of templates from the Re-LDO@G composites by rigid NaOH and HCl treatment did not destroy the interconnected 3D architecture of obtained PGFs (Figure 5a). The graphene units deposited on the secondary template units in Re-LDOs can be assembled into a large flake with the same lateral size and morphology with the original Mg₂Zn_{0.1}Al-LDH flakes and Re-LDO templates (Figure 5a). The

graphene layer number of PGFs is still less than 2, indicating that nanographene units were not recombined and packed into thick graphite layers (Figure 5b). The superior reservation of the CVD-grown few-layer graphene was attributed to the thermally stable nanoparticle templates with a highly curved surface so that the wrapping graphene layer was distorted and difficult to pack. The removal of hard templates rendered PGFs with a highly mesoporous structure constituted of interconnected graphene nanocages (Figure 5c). The hierarchy of mesopores in the graphene assembly is enhanced

by (1) the removal of Re-LDO templates, (2) casting of original mesopores induced by the Kirkendall effect and (3) subsequent volatilization of Zn metal in skeleton of templates (Figure 5d). The mesopores of the 3D graphene derived herein were interconnected with each other, which was attributed to the adjacency of MgO and MgAl₂O₄ template building blocks. The high curvature and 3D interconnection of interior graphene prevented the PGF from stacking graphene routinely adhering to the fringe of the nanoparticles.

In contrast, a Mg-Al template without volatilization of reduced Zn was also employed for the formation of porous graphene. The Zn-free Mg₂Al-LDHs were employed as template precursors, and a large amount of mesosized graphene protuberances cast from the Kirkendall voids acted as spacers to avoid the stacking of graphene layers deposited on both sides of the templates. This resulted in another unstacked double-layer templated graphene (DTG) structure with different topological morphology from PGFs (Figure 5e and Figure S2, Supporting Information).^[9,20]

The PGFs and DTGs exhibited sharp contrast in N₂ sorption capability, indicating the different pore structures (Figure 5f–g). The N₂ isotherms of PGFs and DTGs exhibited a sharp increase at $P/P_0 < 0.05$ and a dominant hysteresis loop at $P/P_0 > 0.35$, indicating a hierarchically micro- and mesoporous structure (Figure 5f). However, higher incremental N₂ sorption at $P/P_0 > 0.45$, and a larger hysteresis loop were observed for PGFs than for DTGs, which confirmed the more dominant mesoporous structure of PGFs, consistent with TEM images (Figure 5d). The SSA_{BET} of PGFs and DTGs were 1448 and 1622 m² g⁻¹, while the pore volumes were 2.44 and 1.55 cm³ g⁻¹, respectively. The calculated pore size distribution of the PGF corroborated the existence of abundant mesopores with sizes of 3–25 nm (Figure 5g). The pore size and volume of PGFs were remarkably higher than DTGs. As summarized in Table S1, Supporting Information, the mesopore volumes of PGFs and DTGs were 2.40 and 1.33 cm³ g⁻¹, respectively, while the SSA contributed by the mesopores was 1326 and 1123 m² g⁻¹ for PGFs and DTGs, respectively. Compared to DTGs, PGFs possessed many more larger sized mesopores and fewer micropores, indicating their much higher electrochemically active surface area and pore volume than that in DTGs.

The unique porous structure of the PGF was induced by enlarged porous Re-LDO templates and consequent defectless curving and interconnecting of graphene structural units. Generally, in Raman spectra of graphene, the G band was assigned to the vibration mode of the ideal graphitic lattice (E_{2g} -symmetry) and the D band was ascribed to the vibration mode of the disordered graphitic lattice and amorphous carbon.^[21] A smaller intensity ratio of D band to G band (I_D/I_G) of 1.95 was obtained for the synthesized PGFs than I_D/I_G of 2.14 for DTGs, indicating the defectless mesoporous structure of PGFs compared to DTGs (Figure S3a, Supporting Information). Although the I_D/I_G ratio of 1.95 reported herein is much higher than that for graphene grown on a Cu substrate (I_D/I_G ratio of 0.03–0.22),^[22] vermiculite (I_D/I_G ratio of 0.94),^[23] MgO templates (I_D/I_G ratio of 0.85)^[24] or ZnO sacrificial scaffolds (I_D/I_G ratio of 1.0),^[13] the SSA and pore volume of PGF reported herein are much

larger than graphene obtained by chemical or thermal reduction of graphene oxide (GO) (100–705 m² g⁻¹, 0.50–1.00 cm³ g⁻¹),^[25] ball-milling graphite (143–437 m² g⁻¹, 0.30–0.50 cm³ g⁻¹),^[26] as well as CVD growth on other hard templates of vermiculite (333 m² g⁻¹, 0.50 cm³ g⁻¹),^[23] and Ni foam templates (300–850 m² g⁻¹, no data on pore volume).^[14] Reducing the dimension of graphene units to less than several tens of nanometers, as well as curving the graphene planes, rendered PGFs with higher I_D/I_G than large-area graphene planes but also higher surface area and more confined pores, which are desirable for applications in electrochemical energy storage.

2.4. Construction of the PGF-S Composites

The use of highly conductive carbon is an effective route to accommodate sulfur as a composite cathode for lithium ion storage.^[27–30] A PGF with large surface area and hierarchically porous structure is expected to be a promising conductive scaffold to accommodate sulfur for Li-S batteries. The PGF-S composite cathodes were fabricated by a facile melt-diffuse method to infiltrate sulfur into the porous structure of the PGF. Both the TEM image and EDX mappings of the PGF-S exhibited a uniform distribution of sulfur in the PGF scaffolds (Figure 6a). As shown in Figure 6b, 63.2 wt% of sulfur in the PGF-S composites exhibited higher thermal stability than bare sulfur, indicating an efficient trapping of sulfur in the porous structure of the PGF scaffold. No clear characteristic peak of elemental sulfur was detected in the XRD patterns and Raman spectra of the PGF-S nanocomposites, further indicating the uniform distribution of sulfur, incorporated with an almost amorphous state (Figure 6c and Figure S3b, Supporting Information). After the infiltration of sulfur, most of the mesopores and all of the micropores of PGFs were occupied by sulfur, resulting in a decreased pore volume of 0.26 cm³ g⁻¹ (Figure 6d).

2.5. Electrochemical Performance of PGF-S Cathode

Li-S cells were fabricated to evaluate the performance of the PGF-S cathodes. The cycling stability of the PGF-S cathodes is illustrated in Figure 7a. An excellent cycling stability was achieved within a potential range of 1.7–2.8 V. An initial discharge capacity of 1187 mAh g⁻¹, corresponding to a very high sulfur utilization of 71%, was achieved for PGF-S cathodes at a current rate of 1.0 C (1.0 C = 1672 mAh g⁻¹, based on sulfur). This capacity rapidly decreased to 1063 mAh g⁻¹ after one cycle, which was attributed to the loss of sulfur during the initial formation of a solid electrolyte interphase at the surface of the lithium anodes. Then, the capacity remained 852 mAh g⁻¹ after 500 cycles, which corresponds to a capacity fading of only ≈20% and a decay rate of ≈0.04% per cycle since the second cycle. In contrast, the initial discharge capacity of DTG-S cathodes was 1086 mAh g⁻¹, which slightly dropped to 1030 mAh g⁻¹ at the second cycle, while only a capacity of 634 mAh g⁻¹ was preserved after 500 cycles, which corresponded to a capacity decay of ≈38% and fading rate of ≈0.08% per cycle. As the PGF-S and DTG-S cathodes

had similar sulfur loading amounts and a uniform distribution of incorporated sulfur (Figure S4, Supporting Information), the gap of their cycling stabilities was mainly induced by the huge difference in porous structures between PGFs and DTGs.

The detailed lithium ion storage performance of PGF-S and DTG-S cathodes was further illustrated by galvanostatic charge-discharge curves. There were two typical voltage plateaus at ≈ 2.3 and ≈ 2.0 V, corresponding to the reduction of sulfur into soluble lithium polysulfides (Li_2S_n , $4 < n < 8$) and the liquid-solid conversion of polysulfides to insoluble $\text{Li}_2\text{S}_2/\text{Li}_2\text{S}$ (Figure 7b).^[31] Herein, the PGF-S and DTG-S cathode at the 3rd cycle exhibited similar discharge capacity and charge behavior. After 500 cycles, the PGF-S exhibited much more significant capacity retention than the DTG-S, especially in terms of the capacity of the high voltage plateau, indicating less sulfur was available for electrochemical reduction in cycled DTG-S cathodes. The superior cycling stability of PGF-S cathodes was mainly aroused from the larger mesopore volume of PGFs than DTGs, which was more favorable for accommodating the volume expansion from sulfur to Li_2S when we considered the similar sulfur content in the whole cathode (Table S1, Supporting Information). Meanwhile, the mesopores with larger size in the PGF

could facilitate the ion diffusion even after prolonged cycling for 500 cycles with inevitable solid deposition in the pores of the carbon scaffolds.

The rate performance of the PGF-S cathode is illustrated in Figure 7c. With the current density increased from 0.1 to 10.0 C, the capacity decreased gradually. A reversible capacity of $\approx 609 \text{ mAh g}^{-1}$ was still preserved at a very high current density of 5.0 C, indicating a superior rate capability of the PGF-S cathode. After harsh cycling at a rather high rate of 10.0 C, the PGF-S cathodes still delivered a high capacity of $\approx 980 \text{ mAh g}^{-1}$ when the current density returned to 0.1 C. The interconnected mesoporous architecture improved electrolyte immersion and diffusion, rendering PGF-S cathodes with extraordinary rate performances.

The superior lithium ion storage performance of the PGF-based sulfur electrode was attributed to the following aspects: (1) The mesoporous PGF with highly conductive graphene building blocks rendering intimate contact to sulfur species, which guaranteed high sulfur utilization of 71% (corresponding to 1187 mAh g^{-1}) at a high current density of 1.0 C; (2) the large hollow cavity of PGFs with significant contribution of large mesopores accommodating the volume expansion of sulfur, leading to superior cycling stability of $\approx 80\%$ over 500 cycles; (3) robust electron pathways

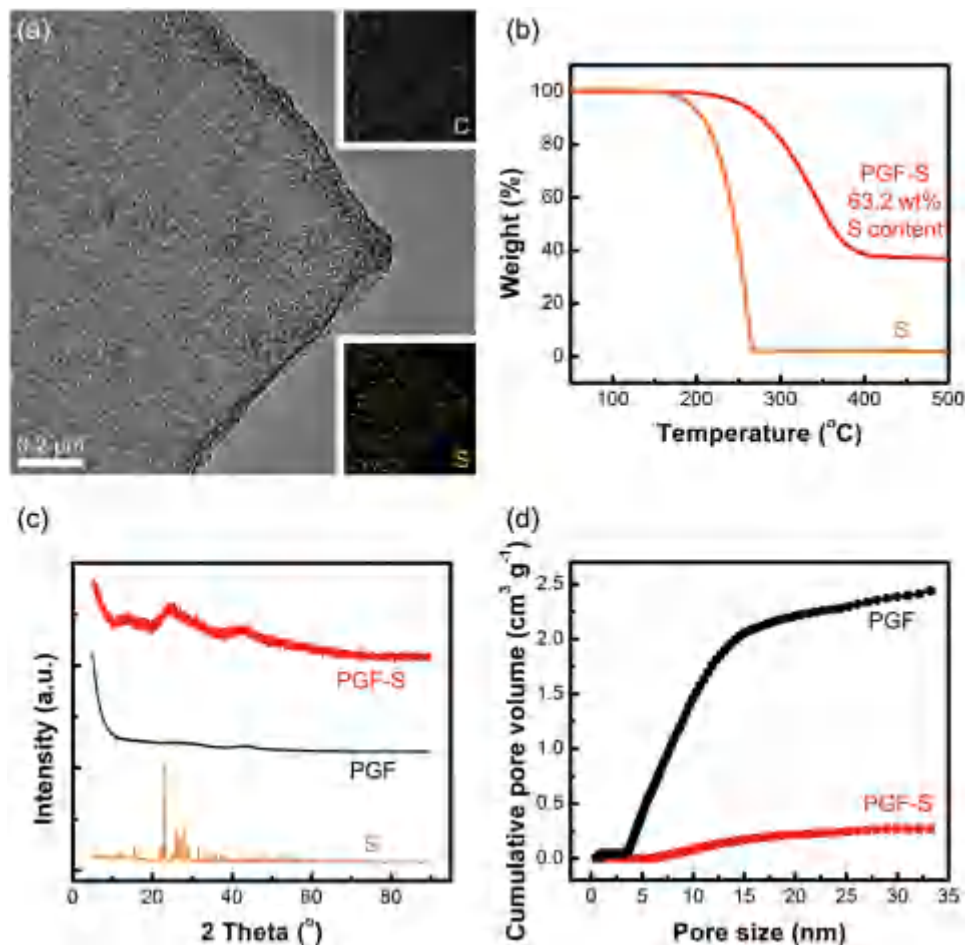


Figure 6. Characterization of the PGF-S nanocomposites. a) TEM image and EDX mappings of the PGF-S nanocomposites, b) the N_2 TGA curve of the PGF-S nanocomposites, c) XRD spectra and d) cumulative pore volume of the PGF before and after the infiltration of sulfur.

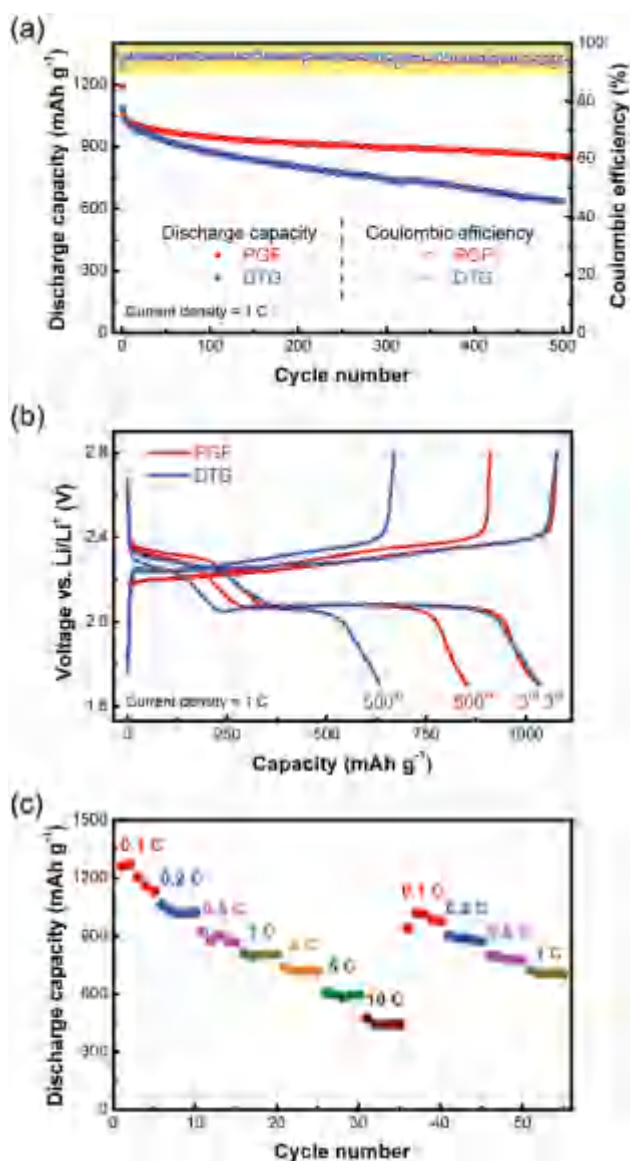


Figure 7. Li-S battery performance of PGF-S cathodes. a) The cycling performance and b) galvanostatic charge/discharge curves of PGF-S cathodes and DTG-S cathodes, c) the rate performance of PGF-S cathodes.

in graphene walls of the PGFs, as well as 3D interconnected macro/mesopores as ion channels for rapid transportation of lithium ions, resulting in 48.4% retention when the current density increased from 0.1 to 5.0 C; and (4) highly chemically and mechanically robust PGF carbon skeletons for long-term durability. Compared with DTG,^[9] CVD graphene,^[15,29] reduced graphene oxide,^[31] cetyltrimethyl ammonium bromide-modified sulfur-graphene oxide,^[32] nitrogen-doped graphene,^[33] porous carbon,^[34,35] CNTs,^[28,36] or their hybrids,^[7,30,37,38] the PGF reported herein is a novel nano-reactor for electrochemical reactions requiring large volume change toleration, high surface area, interconnected electron highways and ion diffusion channels, and that benefit from the introduction of an abundance of large mesopores (3–25 nm) into 3D graphene frameworks. The combination of Kirkendall diffusion and the evaporation of volatile metal

is an effective route to fabricate hierarchical oxide templates for CVD assembly of PGFs with anticipated large mesopores. The modification of graphene-based materials through heteroatom doping^[33,34,38,39] and interfacial mediators (e.g., cetyltrimethyl ammonium bromide,^[32] polyethylene glycol,^[40] and other sulphophilic hosts) is quite promising to enhance their ability for robust hosting of sulfur in a Li-S cell. The battery performance of PGFs is expected to be fully demonstrated through the design of structured electrodes with high areal loading, rational selection of an electrolyte with an anode protector and shuttle inhibitor,^[41] the use of a separator with intelligent ion selectivity and high throughput,^[42] as well as through the applications of a stable anode with robust solid electrolyte interphases^[43] for Li-S cells with very high sulfur utilization and a superior cycle life.

3. Conclusions

A Zn-Mg-Al LDH was selected as a model precursor to fabricate hierarchical oxide templates with small pores induced by Kirkendall diffusion and large pores attributed to the evaporation of a volatile metal. 3D porous graphene was cast onto the Re-LDO templates and obtained after chemical etching of the oxide templates. The obtained PGFs had a high SSA of 1448 m² g⁻¹, 91.6% of which was contributed by mesopores, and a mesopore volume of 2.40 cm³ g⁻¹. This showed a much more mesopore-dominated structure than DTGs grown on Zn-free Mg-Al-LDO templates, with a mesopore volume of 1.33 cm³ g⁻¹ and a SSA contributed by the mesopores of 1123 m² g⁻¹. When the PGFs were applied as the conductive scaffolds for the sulfur cathode in a Li-S cell, a very high initial discharge capacity of 1187 mAh g⁻¹ and a sulfur utilization of 71% were achieved at a current rate of 1.0 C. The capacity decreased to 852 mAh g⁻¹ after 500 cycles, which represented a capacity fading of ≈20% and a fading rate of ≈0.04% per cycle since the second cycle. The rate performance also had a remarkably high capacity of 609 mAh g⁻¹ at 5.0 C. Such excellent cycling stability and rate performance were attributed to the abundance of large mesopores for storage and confinement of sulfur/polysulfides. This work also provides a general strategy of volatile-metal-induced mesopore construction with a view toward the design of hierarchical nanomaterials for promising applications in not only energy storage, but also catalysis, separation, drug delivery, and electrocatalysis.

4. Experimental Section

Template Precursor Preparation: A urea-assisted coprecipitation method was employed to prepare the Mg₂Zn_{0.1}Al-LDH template precursors with a lateral size of ≈4.0 μm. Typically, Mg(NO₃)₂·6H₂O, Al(NO₃)₃·9H₂O, Zn(NO₃)₂·6H₂O, and urea were dissolved in 750 mL deionized water with [Al³⁺] = 0.050 mol L⁻¹, n(Mg²⁺) : n(Zn²⁺):n(Al³⁺) = 2:0.1:1, [urea] = 3.0 mol L⁻¹. The obtained solution was transferred to a 2000 mL glass flask (equipped with a reflux condenser) and was kept at 100 °C under continuous magnetic stirring for 12.0 h. Following that, the suspension was maintained without stirring at 94 °C for 12.0 h.

Mg₂Zn_{0.1}Al-LDHs (representing $n(\text{Mg}^{2+}):n(\text{Zn}^{2+}):n(\text{Al}^{3+})$ in LDH synthetic formula was 2:0.1:1) were finally collected after filtering, washing, and 100 °C-drying of the above suspension.

The control sample of Mg₂Al-LDH flakes with a lateral size of ≈4.0 μm was prepared by a hydrothermal method.^[44] In typical synthesis, an aqueous solution (80 mL) of Mg(NO₃)₂·6H₂O (0.02 mol), Al(NO₃)₃·9H₂O (0.01 mol), and hexamethylenetetramine (0.026 mol) was sealed into a 200 mL autoclave and heated at 140 °C for 24.0 h. The as-synthesized Mg₂Al-LDHs (representing the $n(\text{Mg}^{2+}):n(\text{Al}^{3+})$ in LDH synthetic formula was 2:1) were filtered, washed well with deionized water, and dried at 100 °C for 24.0 h.

Synthesis of PGF and DTG: The PGF was prepared by CH₄-CVD growth with Re-LDOs as the templates in a quartz fixed-bed reactor. Take the preparation of PGF, for example: the LDOs were obtained by calcination of Mg₂Zn_{0.1}Al-LDH flakes at a rate of 30 °C min⁻¹ to 950 °C under flowing Ar (200 mL min⁻¹) and kept at that temperature for 30 min in a horizontal quartz tube reactor for mesoporous generation and expansion. Then H₂ (70 mL min⁻¹) was introduced into the system to reduce ZnAl₂O₄ and evaporate Zn in LDOs for another 30 min at 950 °C. The tailored mesoporous Re-LDO templates without Zn were gained for in situ template CVD growth of graphene by introduction of CH₄ (600 mL min⁻¹). The reaction was maintained for 10 min before the furnace was cooled to room temperature under Ar protection. The DTG was fabricated in a similar way, with template precursors of Zn-free Mg₂Al-LDHs expected.

The raw products were purified by NaOH (15.0 mol L⁻¹) aqueous solution at 180 °C for 12.0 h and HCl (5.0 mol L⁻¹) aqueous solution at 80 °C for 12.0 h sequentially, to fully remove the templates. After filtering, washing, and freeze-drying, both the purified PGF and DTG were finally available.

Fabrication of PGF-S and DTG-S Cathodes: The PGF-S and DTG-S composites were prepared by a facile melt-diffusion strategy. Typically, the mixture containing 35 wt% PGF and 65 wt% sulfur powder was strongly grinded in an agate mortar for 10 min. To completely incorporate the sulfur into the micro-/mesopores of the PGF, the obtained mixture was then placed in a sealed quartz bottle at 155 °C for 1.0 h. The PGF-S cathode slurry was prepared by mixing the PGF-S nanocomposites (80 wt%), CNT conductive agents (10 wt%), and poly(vinylidene fluoride) (PVDF) binder (10 wt%) in an *N*-methylpyrrolidone (NMP) solvent dispersant. Positive electrodes were produced by blade coating the slurry onto aluminum foil and drying at 60 °C for 12.0 h. 13.0 mm diameter disks were punched as the working electrodes for Li-S cells.

Structure Characterizations: The morphology of samples was characterized by a JSM 7401F field-emission scanning electron microscope (SEM, JEOL, Japan) at 3.0 kV and a JEM 2010 high resolution transmission electron microscope (TEM, JEOL, Japan) at 120.0 kV. XRD patterns were recorded on a Bruker D8 Advance diffractometer equipped with a Cu-K_α radiation source. Raman spectra of the DTG samples were collected with a He-Ne laser excitation at 633 nm using LabRAM HR800 Raman spectrophotometer (Horiba Jobin Yvon, France). Thermogravimetric analysis (TGA) was performed by the Mettler Toledo TGA/DSC1 STAR[®] system with a temperature ramp rate of 20 °C min⁻¹. N₂ isotherms were obtained at -196 °C (77 K) with an Autosorb-iQ₂-MP-C system (Quantachrome, USA). The SSA was determined by the BET method. The pore size distribution was calculated using the density functional theory (DFT) method from the adsorption branches of the

isotherms. Before N₂ physisorption measurements, the sample was degassed at the right temperature for 10.0 h to avoid the influence of impurities (a degas temperature of 30 °C for PGF-S and DTG-S and 300 °C for LDO, Re-LDO, PGF, and DTG).

Electrochemical Performance Evaluation: The standard 2025 coin-type cells were employed for electrochemical performance evaluation of PGF and DTG as conductive scaffolds for Li-S batteries. 1.0 mol L⁻¹ lithium bis(trifluoromethanesulfonyl)imide and 1 wt% lithium nitrate dissolved in 1,3-dioxolane/dimethyl ether (with a volume ratio of 1 : 1) was selected as the electrolyte, 1.0 mm thick Li metal foil was used as the anode, and porous Celgard 2400 polypropylene membranes acted as the separator. The areal active materials loading amount is ≈2.4 mg cm⁻². The Li-S cells were assembled in an argon-filled glove-box with 10 μL electrolyte. The coin cells were tested in galvanostatic mode at various currents within a voltage window of 1.7–2.8 V using a Neware multichannel battery cycler. A current density of 1672 mA g⁻¹ (1.0 C) based on the mass of sulfur, which is equivalent to full discharge or charge in 1.0 h, was applied in both current sweep directions. The capacities were calculated on the basis of the mass of sulfur.

Supporting Information

Supporting Information is available from the Wiley Online Library or from the author.

Acknowledgements

This work was supported by the Natural Scientific Foundation of China (No. 21306103, 21422604, and 21561130151), National Basic Research Program of China (2011CB932602 and 2015CB932500), and Tsinghua University Initiative Scientific Research Program (2014z22076). Thanks to Dr. Gui-Li Tian and Dr. Meng-Qiang Zhao for insightful discussion, as well as Rui Zhang for preparing illustrations for this work.

- [1] D. S. Su, R. Schlogl, *ChemSusChem* 2010, 3, 136.
- [2] H. Nishihara, T. Kyotani, *Adv. Mater.* 2012, 24, 4473.
- [3] M. M. Titirici, R. J. White, N. Brun, V. L. Budarin, D. S. Su, F. del Monte, J. H. Clark, M. J. MacLachlan, *Chem. Soc. Rev.* 2015, 44, 250.
- [4] a) D. W. Wang, Q. C. Zeng, G. M. Zhou, L. C. Yin, F. Li, H. M. Cheng, I. R. Gentle, G. Q. M. Lu, *J. Mater. Chem. A* 2013, 1, 9382; b) Y. Yang, G. Y. Zheng, Y. Cui, *Chem. Soc. Rev.* 2013, 42, 3018; c) X. Fang, H. S. Peng, *Small* 2015, 11, 1488; d) A. Manthiram, S. H. Chung, C. X. Zu, *Adv. Mater.* 2015, 27, 1980; e) Z. Li, Y. Huang, L. Yuan, Z. Hao, Y. Huang, *Carbon* 2015, 92, 41; f) J.-G. Wang, K. Xie, B. Wei, *Nano Energy* 2015, 15, 413; g) S. Wu, R. Ge, M. Lu, R. Xu, Z. Zhang, *Nano Energy* 2015, 15, 379.
- [5] J. Y. Luo, H. D. Jang, T. Sun, L. Xiao, Z. He, A. P. Katsoulidis, M. G. Kanatzidis, J. M. Gibson, J. X. Huang, *ACS Nano* 2011, 5, 8943.
- [6] L. Jiang, Z. Fan, *Nanoscale* 2014, 6, 1922.
- [7] M. Q. Zhao, X. F. Liu, Q. Zhang, G. L. Tian, J. Q. Huang, W. C. Zhu, F. Wei, *ACS Nano* 2012, 6, 10759.

- [8] a) Z. J. Fan, J. Yan, L. J. Zhi, Q. Zhang, T. Wei, J. Feng, M. L. Zhang, W. Z. Qian, F. Wei, *Adv. Mater.* 2010, 22, 3723; b) F. Du, D. S. Yu, L. M. Dai, S. Ganguli, V. Varshney, A. K. Roy, *Chem. Mater.* 2011, 23, 4810; c) R. Lv, E. Cruz-Silva, M. Terrones, *ACS Nano* 2014, 8, 4061; d) D. T. Pham, T. H. Lee, D. H. Luong, F. Yao, A. Ghosh, V. T. Le, T. H. Kim, B. Li, J. Chang, Y. H. Lee, *ACS Nano* 2015, 9, 2018; e) C. Tang, Q. Zhang, M. Q. Zhao, J. Q. Huang, X. B. Cheng, G. L. Tian, H. J. Peng, F. Wei, *Adv. Mater.* 2014, 26, 6100.
- [9] M.-Q. Zhao, Q. Zhang, J.-Q. Huang, G.-L. Tian, J.-Q. Nie, H.-J. Peng, F. Wei, *Nat. Commun.* 2014, 5, 3410.
- [10] Y. Zhu, S. Murali, M. D. Stoller, K. J. Ganesh, W. Cai, P. J. Ferreira, A. Pirkle, R. M. Wallace, K. A. Cychosz, M. Thommes, D. Su, E. A. Stach, R. S. Ruoff, *Science* 2011, 332, 1537.
- [11] a) F. Cesano, M. M. Rahman, S. Bertarione, J. G. Vitillo, D. Scarano, A. Zecchina, *Carbon* 2012, 50, 2047; b) P. Strubel, S. Thieme, T. Biemelt, A. Helmer, M. Oschatz, J. Brückner, H. Althues, S. Kaskel, *Adv. Funct. Mater.* 2015, 25, 287.
- [12] C. Wang, M. J. O'Connell, C. K. Chan, *ACS Appl. Mater. Interfaces* 2015, 7, 8952.
- [13] M. Mecklenburg, A. Schuchardt, Y. K. Mishra, S. Kaps, R. Adelung, A. Lotnyk, L. Kienle, K. Schulte, *Adv. Mater.* 2012, 24, 3486.
- [14] Z. P. Chen, W. C. Ren, L. B. Gao, B. L. Liu, S. F. Pei, H. M. Cheng, *Nat. Mater.* 2011, 10, 424.
- [15] Z. Lyu, D. Xu, L. Yang, R. Che, R. Feng, J. Zhao, Y. Li, Q. Wu, X. Wang, Z. Hu, *Nano Energy* 2015, 12, 657.
- [16] H. J. Peng, J. Y. Liang, L. Zhu, J. Q. Huang, X. B. Cheng, X. F. Guo, W. P. Ding, W. C. Zhu, Q. Zhang, *ACS Nano* 2014, 8, 11280.
- [17] a) C. M. Li, M. Wei, D. G. Evans, X. Duan, *Small* 2014, 10, 4469; b) G. Fan, F. Li, D. G. Evans, X. Duan, *Chem. Soc. Rev.* 2014, 43, 7040.
- [18] a) Q. Wang, D. O'Hare, *Chem. Rev.* 2012, 112, 4124; b) M. Q. Zhao, Q. Zhang, J. Q. Huang, F. Wei, *Adv. Funct. Mater.* 2012, 22, 675.
- [19] G.-L. Tian, M.-Q. Zhao, B. Zhang, Q. Zhang, W. Zhang, J.-Q. Huang, T.-C. Chen, W.-Z. Qian, D. S. Su, F. Wei, *J. Mater. Chem. A* 2014, 2, 1686.
- [20] G.-L. Tian, Q. Zhang, M.-Q. Zhao, H.-F. Wang, C.-M. Chen, F. Wei, *AIChE J.* 2015, 61, 747.
- [21] A. Sadezky, H. Muckenhuber, H. Grothe, R. Niessner, U. Poschl, *Carbon* 2005, 43, 1731.
- [22] a) T. Ma, W. Ren, Z. Liu, L. Huang, L.-P. Ma, X. Ma, Z. Zhang, L.-M. Peng, H.-M. Cheng, *ACS Nano* 2014, 8, 12806; b) Y. Zhu, L. Li, C. Zhang, G. Casillas, Z. Sun, Z. Yan, G. Ruan, Z. Peng, A.-R. O. Raji, C. Kittrell, R. H. Hauge, J. M. Tour, *Nat. Commun.* 2012, 3, 1225; c) Z. Z. Sun, A. R. O. Raji, Y. Zhu, C. S. Xiang, Z. Yan, C. Kittrell, E. L. G. Samuel, J. M. Tour, *ACS Nano* 2012, 6, 9790.
- [23] G. Q. Ning, C. G. Xu, Y. M. Cao, X. Zhu, Z. M. Jiang, Z. J. Fan, W. Z. Qian, F. Wei, J. S. Gao, *J. Mater. Chem. A* 2013, 1, 408.
- [24] H. Wang, X. Sun, Z. Liu, Z. Lei, *Nanoscale* 2014, 6, 6577.
- [25] a) Y. Zhao, C. G. Hu, Y. Hu, H. H. Cheng, G. Q. Shi, L. T. Qu, *Angew. Chem. Int. Ed.* 2012, 51, 11371; b) S. Stankovich, D. A. Dikin, R. D. Piner, K. A. Kohlhaas, A. Kleinhammes, Y. Jia, Y. Wu, S. T. Nguyen, R. S. Ruoff, *Carbon* 2007, 45, 1558; c) J. Yan, Q. Wang, T. Wei, L. L. Jiang, M. L. Zhang, X. Y. Jing, Z. J. Fan, *ACS Nano* 2014, 8, 4720; d) C. M. Chen, Q. Zhang, M. G. Yang, C. H. Huang, Y. G. Yang, M. Z. Wang, *Carbon* 2012, 50, 3572; e) M. D. Stoller, S. J. Park, Y. W. Zhu, J. H. An, R. S. Ruoff, *Nano Lett.* 2008, 8, 3498.
- [26] a) I. Y. Jeon, S. Zhang, L. P. Zhang, H. J. Choi, J. M. Seo, Z. H. Xia, L. M. Dai, J. B. Baek, *Adv. Mater.* 2013, 25, 6138; b) I. Y. Jeon, H. J. Choi, S. M. Jung, J. M. Seo, M. J. Kim, L. M. Dai, J. B. Baek, *J. Am. Chem. Soc.* 2013, 135, 1386.
- [27] a) H. J. Peng, J. Q. Huang, M. Q. Zhao, Q. Zhang, X. B. Cheng, X. Y. Liu, W. Z. Qian, F. Wei, *Adv. Funct. Mater.* 2014, 24, 2772; b) M. Q. Zhao, M. Sedran, Z. Ling, M. R. Lukatskaya, O. Mashtalir, M. Ghidui, B. Dyatkin, D. J. Tallman, T. Djenizian, M. W. Barsoum, Y. Gogotsi, *Angew. Chem. Int. Ed.* 2015, 54, 4810; c) G. Zhou, Y. Zhao, A. Manthiram, *Adv. Energy Mater.* 2015, 5, 1402263.
- [28] K. Xi, B. Chen, H. Li, R. Xie, C. Gao, C. Zhang, R. V. Kumar, J. Robertson, *Nano Energy* 2015, 12, 538.
- [29] G. Zhou, L. Li, C. Ma, S. Wang, Y. Shi, N. Koratkar, W. Ren, F. Li, H.-M. Cheng, *Nano Energy* 2015, 11, 356.
- [30] F. Wu, J. Qian, R. Chen, T. Zhao, R. Xu, Y. Ye, W. Li, L. Li, J. Lu, K. Amine, *Nano Energy* 2015, 12, 742.
- [31] J. Q. Huang, X. F. Liu, Q. Zhang, C. M. Chen, M. Q. Zhao, S. M. Zhang, W. C. Zhu, W. Z. Qian, F. Wei, *Nano Energy* 2013, 2, 314.
- [32] M. K. Song, Y. G. Zhang, E. J. Cairns, *Nano Lett.* 2013, 13, 5891.
- [33] C. Wang, K. Su, W. Wan, H. Guo, H. H. Zhou, J. T. Chen, X. X. Zhang, Y. H. Huang, *J. Mater. Chem. A* 2014, 2, 5018.
- [34] J. X. Song, T. Xu, M. L. Gordin, P. Y. Zhu, D. P. Lv, Y. B. Jiang, Y. S. Chen, Y. H. Duan, D. H. Wang, *Adv. Funct. Mater.* 2014, 24, 1243.
- [35] a) J. Liu, T. Y. Yang, D. W. Wang, G. Q. M. Lu, D. Y. Zhao, S. Z. Qiao, *Nat. Commun.* 2013, 4, 2798; b) J. H. Kim, T. Kim, Y. C. Jeong, K. Lee, K. T. Park, S. J. Yang, C. R. Park, *Adv. Energy Mater.* 2015, 5, 1500268; c) C. Hoffmann, S. Thieme, J. Bruckner, M. Oschatz, T. Biemelt, G. Mondin, H. Althues, S. Kaskel, *ACS Nano* 2014, 8, 12130.
- [36] a) X. B. Cheng, J. Q. Huang, Q. Zhang, H. J. Peng, M. Q. Zhao, F. Wei, *Nano Energy* 2014, 4, 65; b) M. Hagen, D. Hanselmann, K. Ahlbrecht, R. Maça, D. Gerber, J. Tübke, *Adv. Energy Mater.* 2015, 5, 1401986.
- [37] a) Q. Li, Z. A. Zhang, Z. P. Guo, Y. Q. Lai, K. Zhang, J. Li, *Carbon* 2014, 78, 1; b) L. Zhu, H. J. Peng, J. Y. Liang, J. Q. Huang, C. M. Chen, X. F. Guo, W. C. Zhu, P. Li, Q. Zhang, *Nano Energy* 2015, 11, 746.
- [38] J. X. Song, M. L. Gordin, T. Xu, S. R. Chen, Z. X. Yu, H. Sohn, J. Lu, Y. Ren, Y. H. Duan, D. H. Wang, *Angew. Chem. Int. Ed.* 2015, 54, 4325.
- [39] H. J. Peng, T. Z. Hou, Q. Zhang, J. Q. Huang, X. B. Cheng, M. Q. Guo, Z. Yuan, L. Y. He, F. Wei, *Adv. Mater. Interfaces* 2014, 1, 1400227.
- [40] S. M. Zhang, Q. Zhang, J. Q. Huang, X. F. Liu, W. C. Zhu, M. Q. Zhao, W. Z. Qian, F. Wei, *Part. Part. Syst. Char.* 2013, 30, 158.
- [41] D. Aurbach, E. Pollak, R. Elazari, G. Salitra, C. S. Kelley, J. Affinito, *J. Electrochem. Soc.* 2009, 156, A694.
- [42] a) J. Q. Huang, Q. Zhang, H. J. Peng, X. Y. Liu, W. Z. Qian, F. Wei, *Energy Environ. Sci.* 2014, 7, 347; b) G. M. Zhou, L. Li, D. W. Wang, X. Y. Shan, S. F. Pei, F. Li, H. M. Cheng, *Adv. Mater.* 2015, 27, 641.
- [43] R. Cao, W. Xu, D. Lv, J. Xiao, J.-G. Zhang, *Adv. Energy Mater.* 2015, 5, 1402273.
- [44] L. Li, R. Ma, Y. Ebina, N. Iyi, T. Sasaki, *Chem. Mater.* 2005, 17, 4386.

Received: May 25, 2015

Revised: June 18, 2015

Published online: August 12, 2015